Review

Check for updates

Author for correspondence:
P. W. Hess   e-mail: pwhess@umd.edu

Present addresses:
*Department of Physics, Middlebury College, Middlebury, VT 05753, USA.
†Northrop Grumman Corporation, Linthicum, MD 21090, USA.
‡Honeywell, Broomfield, CO 80021, USA.
§Department of Physics, Indiana University, Bloomington, IN 47405, USA.
¶Institute for Quantum Computing, and Department of Physics and Astronomy, University of Waterloo, Waterloo, Ontario, Canada N2L 3G1.
#Institute for Defense Analyses, Alexandria, VA 22311, USA.

Non-thermalization in trapped atomic ion spin chains

P. W. Hess*, P. Becker, H. B. Kaplan, A. Kyprianidis,
A. C. Lee†, B. Neyenhuis‡, G. Pagano,
P. Richerme§, C. Senko¶, J. Smith#,
W. L. Tan, J. Zhang and C. Monroe

Joint Quantum Institute, Department of Physics, University of Maryland and National Institute of Standards and Technology, College Park, MD 20742, USA

iD PWH, 0000-0003-2985-4221

Linear arrays of trapped and laser-cooled atomic ions are a versatile platform for studying strongly interacting many-body quantum systems. Effective spins are encoded in long-lived electronic levels of each ion and made to interact through laser-mediated optical dipole forces. The advantages of experiments with cold trapped ions, including high spatio-temporal resolution, decoupling from the external environment and control over the system Hamiltonian, are used to measure quantum effects not always accessible in natural condensed matter samples. In this review, we highlight recent work using trapped ions to explore a variety of non-ergodic phenomena in long-range interacting spin models, effects that are heralded by the memory of out-of-equilibrium initial conditions. We observe long-lived memory in static magnetizations for quenched many-body localization and prethermalization, while memory is preserved in the periodic oscillations of a driven discrete time crystal state.

This article is part of the themed issue 'Breakdown of ergodicity in quantum systems: from solids to synthetic matter'.

1. Introduction

It is well known that highly complex, nonlinear and chaotic classical systems will typically reach a thermal equilibrium state [1]. It is natural to ask how generic this phenomenon might be and whether it can be applied to quantum systems. Of particular interest is the extent

to which thermalization occurs in closed quantum systems, where many of the requirements for classical ergodicity do not apply [2–4]. These questions have led to an extensive body of theoretical work for understanding and classifying the differences between thermalizing and non-thermalizing quantum systems. Much of this is based on the eigenstate thermalization hypothesis [5–7], which predicts that generic observables in strongly interacting quantum systems exhibit thermal properties in their massively entangled eigenstates. There are notable exceptions, like many-body localization (MBL), in which systems fail to thermalize despite strong interactions between constituent particles [8–10]. New analytic and numerical techniques have been developed [3,11–13] to make predictions about these highly excited and out-of-equilibrium quantum states, where the typical tools of statistical physics do not apply.

As with any field of scientific inquiry, experimental measurements are required to confirm these predictions and improve the theoretical tools. Experimental studies using synthetic quantum matter made of trapped and cooled atoms have demonstrated remarkable versatility to study many of these engineered non-ergodic theories [14–19]. These experiments benefit from a high degree of isolation from thermal environments, making them excellent models for closed quantum systems. A broad range of tunable Hamiltonians can be generated using externally applied electromagnetic radiation. Often these optical or microwave radiation fields can be extinguished rapidly, allowing access to highly excited but coherent quantum state dynamics via quench or Floquet processes.

This review will focus on recent experiments that have been performed with linear crystals of trapped atomic ions. Such systems can be used to realize long-range transverse field Ising models (TFIMs) in one dimension (1D) by encoding an effective spin in the internal states of each ion. It is possible to access both chaotic and non-ergodic regimes by controlling interaction strength and range, applying axial or transverse magnetic fields and generating local magnetic field disorder. In §2, we begin with an overview of experimental tools for generating all relevant terms in these long-range Ising models. In §§3 and 4, we discuss observations of MBL in the presence of disorder and prethermalization of spin excitations in clean long-range interacting systems. Both are examples of long-lived memory of initial conditions, a hallmark of non-ergodicity. Finally, in §5, we discuss the observation of a discrete time crystal (DTC), a new non-equilibrium phase of matter with robust and long-lived temporal periodicity, followed by future directions in §6.

2. Tools for quantum simulation with trapped ions

Single-site addressability [20,21], long-range entanglement [22,23] and high-fidelity readout techniques [24,25] make trapped atomic ions a versatile platform for both quantum computation [26] and simulation [27]. Effective spins are encoded in internal electronic levels in each trapped atom. The Coulomb force strongly couples the motional states of ions and provides the mechanism for long-range spin–spin coupling via laser-mediated spin–phonon interactions [28,29].

In particular, the experiments outlined in this review were performed on chains of ^{171}Yb$^+$ in linear radio-frequency (Paul) traps [30]. Effective spins are encoded in the ^{2}S$_{1/2}$ hyperfine ground states of ^{171}Yb$^+$, which we will label $|\uparrow\rangle_z \equiv |F = 1, m_F = 0\rangle$ and $|\downarrow\rangle_z \equiv |F = 0, m_F = 0\rangle$ [31]. A laser tuned to 369.5 nm strongly couples the ground ^{2}S$_{1/2}$ and excited ^{2}P$_{1/2}$ states and is used for state initialization and readout (figure 1c). Trapped ion motion is cooled into the Lamb–Dicke regime by laser cooling, and the spins can be polarized using an optical pumping transition. Imaging the ions with spin-dependent fluorescence allows high-fidelity readout with short exposure times [32] (figure 1b).

(a) Generating long-range transverse field Ising interactions

We perform coherent operations on the ^{171}Yb$^+$ qubits using stimulated Raman transitions. Two overlapped laser beams at 355 nm provide a momentum transfer Δk along the transverse direction of the ion chain (figure 1a). If the beatnote between them is resonant with the qubit
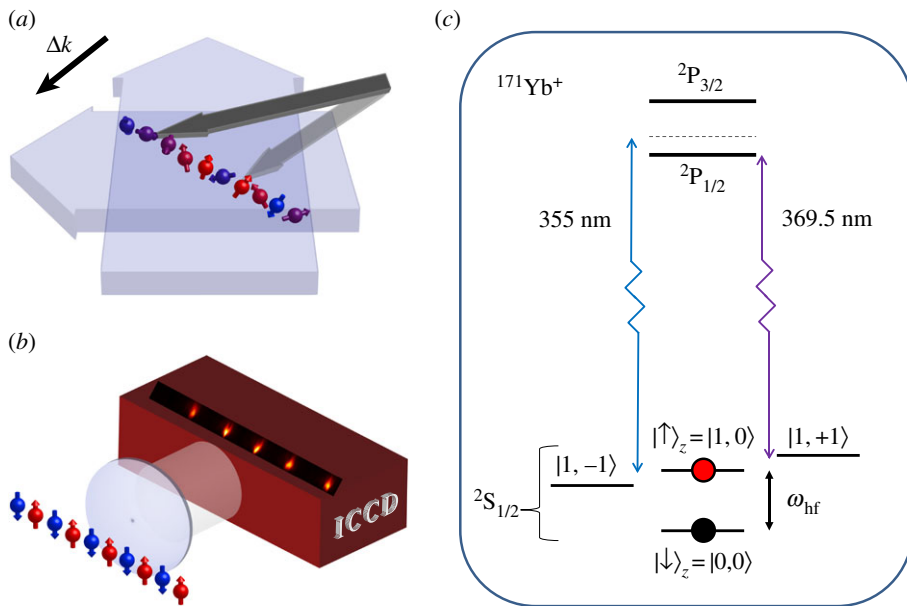
Figure 1. Experimental schematic. (*a*) A 1D chain of trapped ion spins evolves under the influence of global Raman beams (broad blue arrows) which generate long-range transverse field Ising interactions. Local disorder can be realized by rastering a tightly focused individual addressing laser (grey arrows) across selected ions. (*b*) Ion magnetizations $\langle \sigma_i^z \rangle$ are imaged through state-dependent fluorescence on an intensified charge-coupled device camera (ICCD). (*c*) Energy level diagram of $^{171}\mathrm{Yb}^+$. The ground-state manifold has four sublevels, but the two picked for the qubit states $| \uparrow \rangle_z$ and $| \downarrow \rangle_z$ are magnetically insensitive 'clock states'.

frequency ($\omega_{\mathrm{hf}}/2\pi = 12.642819\,\mathrm{GHz}$), then the spins are coherently rotated with a two-photon Rabi frequency $\Omega \sim 1\,\mathrm{MHz}$. Resolved sideband interactions between spin and motion result if the beatnote is detuned from the qubit frequency by an amount μ near the motional frequencies ω_m, provided we are in the Lamb–Dicke regime $\eta = \Delta k\sqrt{\hbar/(2M\omega_m)} \ll 1$, for ion mass M.

Effective spin–spin interactions are engineered with an off-resonantly driven optical dipole force [28]. Stimulated Raman transitions with a bichromatic beatnote detuning $\pm\mu$ generate an evolution operator

$$U(t) = \exp\left[\sum_i \hat{\phi}_i(t)\sigma_i^x + \mathrm{i}\sum_{i,j} \chi_{i,j}(t)\sigma_i^x\sigma_j^x \right]. \tag{2.1}$$

Here, $\hat{\phi}_i(t)$ describes spin-dependent displacements of phononic excitations in phase space, while $\chi_{i,j}(t)$ is a phonon-independent spin–spin coupling term [33,34].

We operate in the detuned regime where $|\mu - \omega_m| \gg \eta\Omega$, which keeps $\hat{\phi}_i(t)$ small and bounded. The state evolution is described by an effective Ising Hamiltonian in spin space alone (with $\hbar = 1$)

$$H_{\mathrm{SS}} = \sum_{i<j} J_{i,j}\sigma_i^x\sigma_j^x. \tag{2.2}$$

The interaction matrix $J_{i,j}$ is given by a sum over the ion couplings to all normal modes

$$J_{i,j} = \Omega^2\omega_{\mathrm{R}} \sum_{m=1}^{N} \frac{b_{i,m}b_{j,m}}{\mu^2 - \omega_m^2}, \tag{2.3}$$

where $\omega_{\mathrm{R}} = \hbar\Delta k^2/2M$ is the atomic recoil frequency and $b_{i,m}$ is the normalized eigenmode matrix for motional mode ω_m.

In the experiments described here, the spin–spin interactions are generated by 'global' Raman lasers which apply an equal intensity and beatnote detuning ($\delta_m = \mu - \omega_m$) to each ion. The spin model realized under these conditions takes the form of a power law decaying with distance

$$J_{i,j} \approx \frac{J_0}{|i - j|^\alpha}, \tag{2.4}$$

where J_0 is the average nearest-neighbour strength and α the tunable range. The range can be adjusted continuously from an all-to-all coupling of $\alpha = 0$ when the contribution from the centre-of-mass mode dominates ($\delta_{\mathrm{COM}} \ll \delta_m$) to a short-range dipolar interaction of $\alpha = 3$ as $\delta_m \to \infty$.

For these experiments, the stimulated Raman transitions are driven by a mode-locked tripled Nd:YVO$_4$ laser at 355 nm. The 120 MHz repetition rate and approximately 14 ps pulse width of this laser create a frequency comb with enough bandwidth to span the qubit hyperfine splitting [35]. We tune $J_{i,j}$ by adjusting μ or the trap voltages and are limited to a range of $0.5 < \alpha < 2$ and $J_0/2\pi \leq 1$ kHz by the available laser power and the Paul trap geometry. Tunability of μ and the Rabi frequency ($\Omega(t)$) is provided by an acousto-optic modulator driven by an arbitrary waveform generator, and drifts in the laser's repetition rate are accounted for by stabilizing the beatnote at ω_{hf} using a feedback scheme [36].

Both transverse and axial field Ising models can be realized by adding effective magnetic fields

$$H_B = \frac{B}{2} \sum_i \sigma_i^\gamma, \tag{2.5}$$

where $\gamma = (x, y, z)$. Magnetic fields in $\gamma = (x, y)$ are generated by driving stimulated Raman transitions resonant with the qubit frequency ω_{hf}, in which the phase of this third frequency component with respect to the bichromatic beatnotes determines the field's direction in the xy-plane. Alternatively, by applying a global shift to the bichromatic beatnote frequencies by an amount B, a rotating frame shift between the qubit and the beatnotes generates an effective field in $\gamma = z$ [37]. In either case, we limit $B/2 \ll \eta\Omega \ll \delta_{\mathrm{COM}}$ in order to prevent unwanted higher-order terms in our effective Hamiltonian, practially limiting us to $B/2\pi \leq 10$ kHz.

The particular shape of $J_{i,j}$ and its dependence on δ_m can be verified using a spectroscopic technique [38]. We weakly modulate the transverse magnetic field such that

$$H = \sum_{i<j} J_{i,j}\sigma_i^x \sigma_j^x + (B_0 + B_{\mathrm{P}} \sin(2\pi\nu_p t)) \sum_i \sigma_i^y. \tag{2.6}$$

When the probe frequency ν_{p} is resonant with an energy splitting $\Delta E = |E_a - E_b|$ between eigenstates $|a\rangle$ and $|b\rangle$, the transverse field will drive transitions if there is a non-zero matrix element $\langle b| \sum_i \sigma_i^y |a\rangle \neq 0$. In the case of a weak transverse field, $(B_0, B_{\mathrm{P}}) \ll J_0$, this corresponds to transitions between the eigenstates of $\sum_i \sigma_i^x$ that have a single spin flipped (e.g. $|\uparrow\uparrow \cdots \uparrow\rangle_x$ and $|\downarrow\uparrow \cdots \uparrow\rangle_x$). By scanning the probe frequency and monitoring the population transfer between eigenstates, we can directly measure the eigenstate energy splittings of our many-body Hamiltonian (figure 2a).

For an eigenstate transition that has flipped spin i, the measured energy difference is $\Delta E_i = 2\sum_j J_{i,j}$. Measuring $N(N-1)/2$ energy splittings provides sufficient information to solve this system of equations and extract each component of $J_{i,j}$ (figure 2b,c). We can also use individual addressing to measure components of $J_{i,j}$ by shelving all ions except i,j into dark Zeeman sublevels ($|1,\pm1\rangle$) that do not interact when H_{SS} is applied [39,40]. The oscillation frequency between $|\downarrow_i\downarrow_j\rangle_z \to |\uparrow_i\uparrow_j\rangle_z$ is a direct measurement of $J_{i,j}$. Both techniques have similar scaling with system size to measure $J_{i,j}$ with arbitrary couplings, but the spectroscopic method avoids the additional experimental overhead required for individual addressing. Such a procedure will prove especially useful for verifying more complex $J_{i,j}$ matrices, which can be engineered with individually addressed stimulated Raman interactions [41].
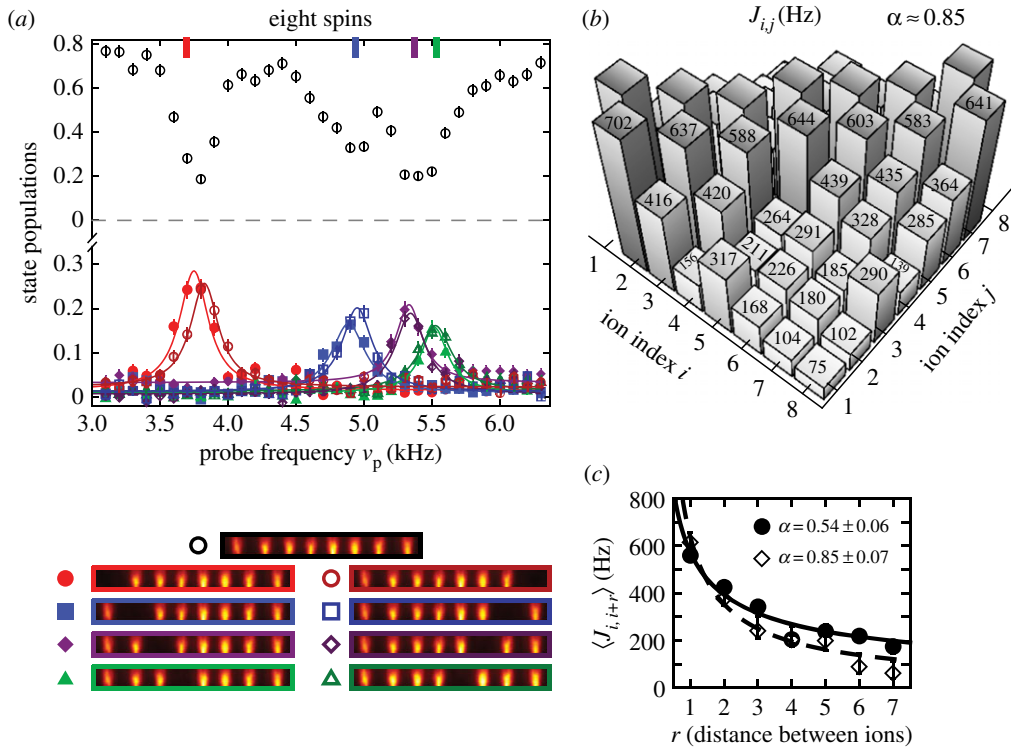
Figure 2. Spectroscopic Hamiltonian measurement. (*a*) Scanning the frequency of a weak, oscillating magnetic field probe ν_p will cause population transfer from an initially polarized state $|\uparrow\uparrow\uparrow\uparrow\uparrow\uparrow\uparrow\uparrow\rangle_x$ to those with a single spin flipped when the probe is resonant with their frequency difference. Depleted population in the initial state is observed simultaneously with an increased population in the excited states. (*b*) Measurement of $N(N-1)/2$ independent frequency splittings is sufficient to invert the many-body spectra and solve for the coupling matrix $J_{i,j}$. (*c*) The average measured interaction range is fitted to a power-law decay in two cases, with good agreement to a range calculated from the trap frequencies and laser beatnote detunings. Adapted from [38].

(b) Individual addressing for state preparation and programmable disorder

A critical tool for realizing a non-ergodic MBL Hamiltonian is the ability to apply controlled disorder to the system. In this case, we apply local effective magnetic fields of the form

$$H_D = \sum_i D_i \sigma_i^z. \tag{2.7}$$

These interactions are generated with a tightly focused 355 nm laser beam which imposes a light shift $2D_i$ on the bare qubit frequency. For $^{171}\mathrm{Yb}^+$ qubits, the differential shift from the second-order AC Stark effect between the $|\uparrow\rangle_z$ and $|\downarrow\rangle_z$ states from 355 nm light is highly suppressed [42]. This is advantageous for maintaining a stable qubit with long coherence time, but makes it difficult to apply disorder using an interaction like H_D. By contrast, individual addressing using the AC Stark effect from a focused laser beam has been demonstrated for alkaline-earth ions, where this suppression is not present [20,43].

When the light field contains coherent frequency components with a frequency difference (δ_2) not far detuned from the qubit frequency, a fourth-order light shift can become significant and dominate over the typical second-order (AC Stark) shifts [21,44]. When $\delta_2 = 0$, this light field drives stimulated Raman transitions with Rabi frequency $\Omega = g_0^2/2\Delta$, where g_0 is the resonant Rabi frequency of the 6S → 6P transition and Δ is the detuning of the 355 nm laser from the $^2\mathrm{P}_{1/2}$

states. The resulting effective interaction can shift the qubit frequency by

$$\delta\omega^{(4)} = \frac{|\Omega|^2}{2\delta_2}. \tag{2.8}$$

The fourth-order shift $\delta\omega^{(4)}$ has a quadratic dependence on the laser intensity since $g_0^2 \propto I$. The relative strength of the fourth-order and second-order light shifts is $\delta\omega^{(4)}/\delta\omega^{(2)} = g_0^2/4\delta_2\omega_{hf}$, which means the fourth-order shift dominates in the limit of high laser intensity $g_0^2 \gg \delta_2\omega_{hf}$.

In our case, these frequency components arise from a mode-locked laser with 120 MHz repetition rate, $|\delta_2| \leq 60$ MHz. With a tight focus, the intensity is sufficiently high that we observe a clear quadratic dependence of the qubit shift on laser intensity [21]. The 355 nm light for individual addressing is focused through our imaging objective lens to achieve a beam waist of a few micrometres. This limits crosstalk between individually addressed ions to less than 2% and provides sufficiently high-fidelity single qubit control for our application.

An acousto-optic deflector (AOD) is used to translate the lateral position of the addressing beam focus and select which ion to address. Although multiple ions can be addressed simultaneously by driving the AOD with multiple frequencies, this leads to an inefficient use of our optical power because of the quadratic intensity dependence of the fourth-order light shift. A linear scaling of $\delta\omega^{(4)}$ per ion can be recovered instead by rastering across all ions to be addressed. In the limit that the raster frequency is much faster than other relevant frequency scales in our quantum simulation, then this simply acts like the desired time-averaged local magnetic field with $D_i = \langle\delta\omega_i^{(4)}\rangle/2$.

A site-dependent light shift can also be used to prepare arbitrary initial product states [45,46]. A Ramsey scheme provides the highest-fidelity technique for flipping individual spins. The spins are optically pumped then rotated into $|\downarrow\rangle_x$, at which time H_D is applied with equal light shifts D to select ions. The light-shifted ions will precess faster and after time $t = \pi/(2D)$ they will be 180° out of phase from the other spins. A final $\pi/2$ pulse then rotates this into a product state diagonal in the z-basis.

3. Many-body localization in a trapped ion spin chain

With the above-described experimental tools, we can study dynamical phenomena in the TFIM and probe its rich quantum phase structure. MBL is an intense field of interest, whereby disorder gives rise to non-ergodic behaviour even in strongly interacting systems [9,10,47]. This effect is a generalization of single-particle 'Anderson' localization [48], which is well understood theoretically and has been measured in a number of experimental platforms [15,49–54]. In Anderson localization, experiments are limited to regimes of low excitation energy and no interparticle interactions. In the case of MBL, non-ergodicity and the absence of thermalization are present at much higher initial energy densities and temperatures, and within a broad set of interaction ranges and disorder strengths.

Although a number of observables have been identified to characterize phase transitions between MBL and ergodic states [55], the main experimental signature probed in trapped ion spin chains is the long-lived memory of initial conditions [56,57]. We begin the experiment by preparing the 10-spin Néel state with staggered order ($|\psi_0\rangle = |\downarrow\uparrow\downarrow\uparrow\downarrow\uparrow\downarrow\uparrow\downarrow\uparrow\rangle_z$) which is highly excited with respect to the disordered Ising Hamiltonian

$$H_{MBL} = \sum_{i<j} J_{i,j}\sigma_i^x\sigma_j^x + \frac{B}{2}\sum_i \sigma_i^z + \sum_i D_i\sigma_i^z, \tag{3.1}$$

where D_i is sampled from a uniform distribution, $D_i \in [-W/2, W/2]$, with width W. This Hamiltonian is rapidly switched on at $t = 0$, and the resulting quench dynamics of the single-spin magnetizations $\langle\sigma_i^z(t)\rangle$ are measured for times up to $t = 10/J_0$.

In the absence of disorder, these same initial spin states will thermalize if the uniform transverse field B is sufficiently large [5–7]. We prepare eigenstates of both σ^x and σ^z and measure
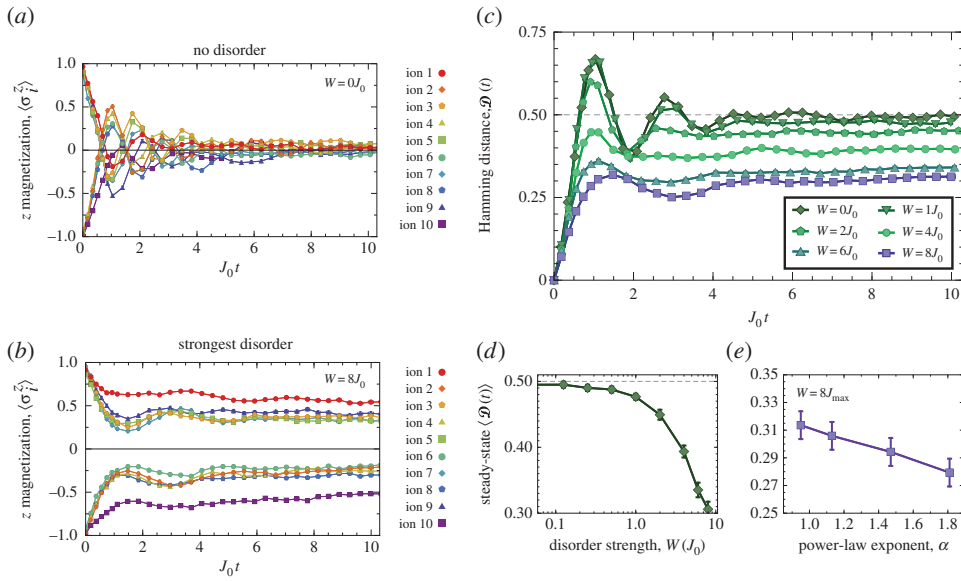
Figure 3. Many-body localization. (*a*) With no disorder present, the prepared Néel state of 10 ions thermalizes to a state consistent with $\langle \sigma_i^z \rangle \approx 0$ for each spin. (*b*) With the strongest achievable disorder, $W = 8J_0$, all spins retain memory of initial conditions with $\langle \sigma_i^z \rangle \neq 0$. (*c*) The normalized Hamming distance $\mathcal{D}(t)$ has reached a steady-state value for $J_0 t \geq 5$ at all measured disorder strengths. (*d*) The time-averaged steady-state value $\langle \mathcal{D}(t) \rangle$ after the plateau exhibits the onset of a crossover between a thermalizing regime ($\langle \mathcal{D}(t) \rangle = 0.5$) and localizing regime ($\langle \mathcal{D}(t) \rangle = 0$). (*e*) The steady-state Hamming distance increases with longer-range interactions, indicative of the movement away from the single-particle Anderson localization limit at $\alpha \to \infty$. In all plots, each time series is an average over 30 instances of disorder. Adapted from [39].

the resulting single-ion magnetization projected into those directions. In the case of a thermalizing system, we expect information of generic initial conditions to be lost in all directions of the Bloch sphere, namely $\langle \sigma_i^x \rangle = \langle \sigma_i^z \rangle = 0$. We observe that the system thermalizes rapidly ($J_0 t < 5$) for values of transverse field $B \geq 4J_0$ (figure 3*a*).

The transverse field is held fixed at $B = 4J_0$ in order to study how disorder localizes the spin (figure 3*b*). Each measurement of magnetization dynamics for disorder width W is repeated with 30 different realizations of disorder, which are subsequently averaged together. This number of realizations is sufficient to reduce the disorder sampling error to be smaller than the features of interest. Averaging over initial states is unnecessary, because MBL applies over a broad range of initial energies which are sampled by the disorder averaging.

We observe that, after some initial growth and oscillations, the magnetization of each spin settles to a steady-state value for $J_0 t \geq 5$. To quantify the degree of localization, we compute the normalized Hamming distance (HD)

$$\mathcal{D}(t) = \frac{1}{2} - \frac{1}{2N} \sum_i \langle \psi_0 | \sigma_i^z(t) \sigma_i^z(0) | \psi_0 \rangle$$

$$= \frac{1}{2} - \frac{1}{2N} \sum_i (-1)^i \langle \sigma_i^z(t) \rangle. \tag{3.2}$$

This counts the number of spin flips from the initial state, normalized to the length of the chain. At long times, a randomly oriented thermal state shows $\mathcal{D} = 0.5$, while one that remains fully localized has $\mathcal{D} = 0$ (figure 3*c*). The average steady-state value $\mathcal{D}(t)$ for $J_0 t \geq 5$ serves as an order parameter for probing the crossover between localizing and thermalizing regimes.

As a function of W, the disorder clearly pushes the spin chain towards a localized regime (figure 3*d*). Likewise, the localization strengthens as α is increased towards shorter-range interactions (figure 3*e*), recovering Anderson localization via a Jordan–Wigner transformation

in the $\alpha \to \infty$ limit. Numerical studies have confirmed that full localization occurs within experimentally accessible disorder strengths and interaction ranges [58]. A many-body delocalization transition predicted at $\alpha > 1.5$ is absent from our data, and is probably due to finite size effects [59]. Characterizing and eliminating these finite size effects is a major goal of future planned experiments using much longer chains of trapped $^{171}\text{Yb}^+$ ions.

MBL is a unique case in which a closed quantum system remains non-ergodic and localized even up to infinite times. Such a prediction is hard to verify experimentally, as there is always some finite coupling to the environment that will thermalize the system over accessible time scales [60,61]. This makes it difficult to distinguish truly MBL phases from those in which the dynamics are glassy or metastable, but will thermalize over long time scales even in a closed system [62].

4. Prethermalization: memory without disorder

While the disordered Hamiltonians necessary for MBL are inherently non-integrable, it is also interesting to study the degree to which integrability breaking can lead to non-ergodic behaviour in clean systems [3,63,64]. The long-range TFIM realized in our trapped ion quantum simulator presents a unique context to study this since the degree of integrability breaking can be tuned via the interaction range [65]. Such nearly integrable systems typically show metastable plateaus where memory of initial conditions is preserved for long, but not infinite, times.

Prethermalization describes the physics of these metastable states and the mechanisms by which they stay out of equilibrium for extended periods of time [66]. Many of the experimental realizations of prethermalization involve nearly integrable systems, such as 1D Bose gases [14, 16,67], which can still be characterized by approximately conserved quantities associated with integrability. The prethermalization, in such cases, is accurately described by relaxation to a distribution given by a generalized Gibbs ensemble (GGE) [68].

By contrast, the long-range interactions realized in our trapped ion quantum simulator create a prethermal state which is sufficiently far from integrability that it cannot be predicted by a GGE [45,69,70]. We analyse this prethermalization using a Holstein–Primakoff transformation, where spin excitations in an Ising chain are mapped to free bosons. For nearest-neighbour interactions with open boundary conditions, these bosons propagate in a square well potential. An increased interaction range raises a potential barrier in the middle of the spin chain, resulting in prethermal confinement of spin excitations created on either side of the barrier (figure 4a). The long-time memory of initial conditions, relaxed by tunnelling through this emergent barrier, is the observed signature of this prethermal state.

The experiment begins by preparing a single spin excitation on either edge of a seven-ion chain $|\psi_R\rangle = |\downarrow\downarrow\downarrow\downarrow\downarrow\downarrow\uparrow\rangle_z$ or $|\psi_L\rangle = |\uparrow\downarrow\downarrow\downarrow\downarrow\downarrow\downarrow\rangle_z$. We then quench on the long-range TFIM Hamiltonian

$$H = \sum_{i<j} J_{i,j}\sigma_i^x\sigma_j^x + B\sum_i \sigma_i^z, \tag{4.1}$$

in the limit where $B \gg J_0$ and for interaction ranges of either $\alpha = 0.55$ (long range) or $\alpha = 1.33$ (short range). In this limit, the strong B field makes it energetically forbidden to create or destroy spin excitations, and the initial spin excitation will propagate ballistically through the spin chain [40,71].

We quantify the position of the spin excitation by measuring the observable

$$C(t) = \sum_i \frac{2i - N - 1}{N - 1}\frac{\sigma_i^z + 1}{2}, \tag{4.2}$$

which ranges from -1 to 1 if the spin excitation is on the left/right side of the chain, respectively. Memory of initial conditions is observed only in the case of long-range interactions, where $\text{sign}(\langle C(t)\rangle) = \text{sign}(\langle C(0)\rangle)$ for times up to $J_0 t = 25$, regardless of initial conditions. The effect is pronounced in the cumulative time average $\langle \bar{C}\rangle$, which averages out high-frequency oscillations. The observed prethermalization is robust to weak interactions between spin excitations. When
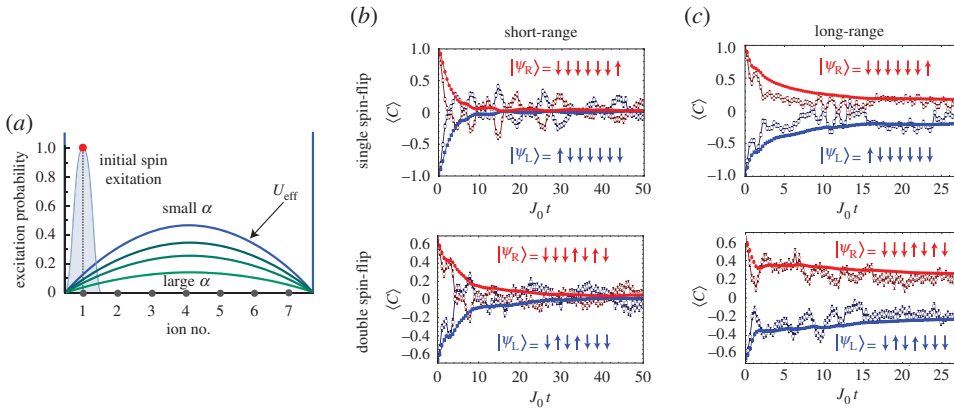
Figure 4. Prethermalization. (*a*) An initial spin excitation is prepared on one side of a seven-ion chain subject to open boundary conditions and long-range *XY* interactions. As the range increases (α decreases), the excitation is subject to an emergent potential barrier. (*b*) In the case of short-range interactions, either one or two spin flips delocalize to $\langle C \rangle \approx 0$, consistent with the GGE. (*c*) For long-range interactions, memory of initial conditions is preserved in a long-lived prethermal state. In both (*b*) and (*c*), the open blue squares or red circles plot $\langle C \rangle$ for initial states prepared on the left or right side of the spin chain, respectively, while the filled blue squares or red circles plot the cumulative time average $\langle \bar{C} \rangle$ for these data. Adapted from [45].

two spin excitations are prepared in $|\psi_0\rangle = |\downarrow\uparrow\downarrow\uparrow\downarrow\downarrow\downarrow\rangle$, which is even further from integrability than the single-spin-flip case, the resulting dynamics are still prethermal in the presence of long-range interactions (figure 4*b*,*c*).

This state should persist in the thermodynamic limit, where the long-range interactions and open boundary conditions continue to effectively break the translational invariance in the bulk. We observed that this effect still persisted when we more than tripled the length of the spin chain to 22 ions. This experiment serves as a good example of non-ergodicity breaking in clean systems and is a clear demonstration that prethermal behaviour cannot always be described using the formalism of the GGE.

5. Discrete time crystals

So far, we have considered cases where a quantum quench to a static Hamiltonian leads to non-ergodic quantum dynamics. Time-dependent or periodic Hamiltonians also support out-of-equilibrium phases with spin dynamics that are either robustly oscillatory and localized in frequency space, or dephase from ergodic evolution [72,73]. Take the example of the quantum kicked rotor, in which the periodic (Floquet) Hamiltonian generates dynamics which can be tuned between chaotic and temporally localizing regimes [74,75]. Many of the robustly oscillatory phases of matter in Floquet systems have no direct analogues to phenomena in quenched static Hamiltonians [76,77].

A discrete (Floquet) time crystal is an example of a non-ergodic time-dependent phase, where symmetry-breaking spin oscillations show robustness to variations in the system Hamiltonian [76, 78–80]. This effect has a close connection to MBL, which is used here as a mechanism to stabilize the time crystal dynamics and prevent heating due to the Floquet drive [72,73,81]. While a static MBL Hamiltonian causes long-lived memory of initial conditions in spin magnetizations, a Floquet MBL Hamiltonian preserves the memory of the initial phase of the oscillatory dynamics.

In the case of a DTC, this long-lived oscillation is also an example of discrete time translational symmetry breaking. A discrete symmetry is imposed on the system by the periodicity T of the Hamiltonian, $H(t) = H(t + T)$. However, the DTC state spontaneously breaks this symmetry by oscillating at a subharmonic frequency with period $2T$. When an MBL Hamiltonian is part of the Floquet drive cycle, the symmetry-breaking is robust to perturbations in the drive. Both the
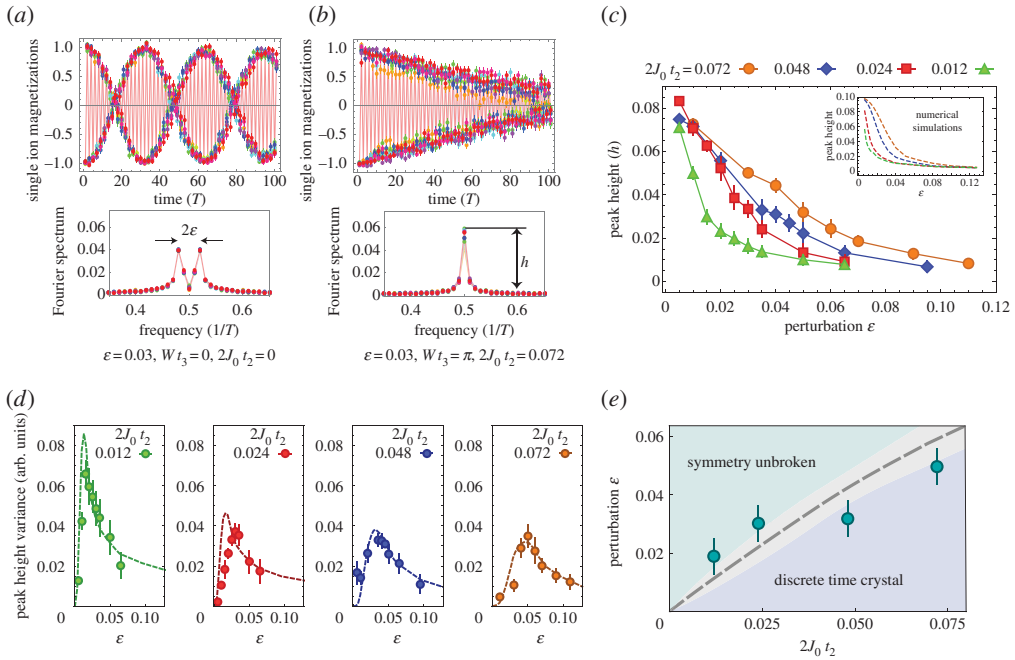
Figure 5. Discrete time crystals. (*a*) Spin dynamics under repeated application of H_1. A perturbation that modifies the frequency response is clearly visible in the Fourier domain by two peaks separated by 2ε. (*b*) When the MBL terms H_2 and H_3 are also applied, all spins oscillate in phase and with a common frequency of $1/(2T)$. (*c*) The height of the Fourier peak h at frequency $1/(2T)$ is used as an order parameter to demonstrate how larger ε destroys the DTC order at four different values of J_0. (*d*) The variance of h diverges at the phase transition boundary for each value of J_0, and exhibits good agreement with numerical predictions (dashed lines). (*e*) The critical ε at the peak of the data in (*d*) demonstrates a linear dependence with $J_0 t_2$. This boundary separates DTC from symmetry-unbroken phases in the thermodynamic limit. Adapted from [86].

symmetry-breaking oscillations and their robustness caused by many-body interactions provide an analogy to spontaneous breaking of spatial symmetry in the formation of solid crystals [82]. The original proposals for observing time crystals in the spontaneous breaking of continuous time translational symmetry in a ground state were shown to be impossible [83–85], but the DTC is a generalization of this concept.

We perform an experiment driving a 10-ion spin chain with a periodic Hamiltonian to realize the DTC [86]. We prepare an initial state polarized in $|\psi_0\rangle = |\downarrow\rangle_x$, then apply a three-component Floquet Hamiltonian with overall period $T = t_1 + t_2 + t_3$,

$$H = \begin{cases} H_1 = g(1 - \varepsilon) \sum_i \sigma_i^y, & \text{time } t_1, \\ H_2 = \sum_{i<j} J_{i,j} \sigma_i^x \sigma_j^x, & \text{time } t_2, \\ H_3 = \sum_i D_i \sigma_i^x & \text{time } t_3, \end{cases} \tag{5.1}$$

where g is the effective Rabi frequency tuned such that $2g t_1 = \pi$ and ε is a fractional perturbation varied between 0 and 15%. We observe the magnetization $\langle \sigma_i^x \rangle$ after each Floquet period T and evolve the system out to 100 periods. The data are analysed in the frequency domain by applying a discrete Fourier transform to the time series, where the expected subharmonic oscillations will occur at a frequency of $\nu_{tc} = 1/(2T)$.

The first term H_1 is a perturbed π pulse which breaks the system's time translational symmetry. In the absence of H_2 and H_3, the spin magnetizations do not generically oscillate at the subharmonic frequency, and the system instead tracks the drive at frequency $\nu = T^{-1}(1/2 - \varepsilon)$

(figure 5a). Terms H_2 and H_3 combined generate a Hamiltonian deep in the MBL regime.[1] The short-range ($\alpha = 1.5$) interactions are weak, $J_0 t_2 < 0.04$, compared with the disorder, which is pulled from a uniform distribution of width W set to $W t_3 = \pi$.

The application of H_2 and H_3 with small ε restores the magnetization oscillations to the subharmonic frequency ν_{tc} (figure 5b). To quantify the degree of temporal ordering, the amplitude of the Fourier transform at the subharmonic frequency $h(\nu_{tc})$ is used as an order parameter (figure 5c). By varying ε and J_0, we can probe the crossover from DTC to symmetry-unbroken phases and observe that the temporal order is destroyed when $\varepsilon \gtrsim 2J_0 t_2$. The variance of $h(\nu_{tc})$, taken across 10 disorder instances, peaks at the crossover boundary, as would be indicative of a phase transition in the thermodynamic limit (figure 5d). The peak of the variance observable exhibits a linear relationship between ε and J_0 as expected, revealing the parameter regime in which the DTC is stable against perturbations (figure 5e).

Discrete time crystals are not specific to 1D spin chains and have also been observed in a three-dimensional crystal of nitrogen vacancy centre spins in diamond [87]. These experiments point to the role that Floquet drives can play in generating entirely new phases of matter, which may not exist in static or equilibrium systems. These states can exhibit a gamut of features like symmetry-protected topological order or non-ergodicity. Understanding all of these regimes will require new theoretical tools for treating highly out-of-equilibrium quantum systems, and complementary experiments on large and strongly interacting systems to verify them.

6. Conclusion and future directions

We have discussed a few contexts where chains of trapped ions, tailored with optical forces to realize strongly interacting spin models, can be made to exhibit non-ergodic many-body quantum dynamics [39,45,86]. There is promise in expanding these studies to observe new examples of non-ergodic phenomena in quench- or Floquet-type experiments. Performing similar experiments in two-dimensional ion crystals would help answer questions about the viability of MBL in more than one dimension [88]. Penning traps have been used to confine large rotating two-dimensional ion crystals with tunable long-range interactions [89,90], but similar crystals created in Paul traps would benefit from improved spatio-temporal resolution for spin initialization and readout [91,92].

Along with the potential to study spatially two-dimensional quantum Ising models with a high degree of spin connectivity, it is also possible to explore how higher-dimensional spins ($S > 1/2$) would affect the observed examples of non-ergodicity. For example, the DTC has modified subharmonic ordering for $S = 1$ systems [80,87], and there might be many other unique effects considering the topological nature of integer-spin Heisenberg chains [93,94]. Integer-spin dynamics have been demonstrated with trapped ^{171}Yb$^+$ atoms [95–97], where three spin states can be encoded if we include additional Zeeman sublevels in the ^{2}S$_{1/2}$ manifold: $|+\rangle = |F = 1, m_F = 1\rangle$, $|-\rangle = |F = 1, m_F = -1\rangle$ and $|0\rangle = |F = 0, m_F = 0\rangle$. We can generate an effective Hamiltonian by applying a bichromatic field with beat frequencies $\omega_- + \mu$ and $\omega_+ - \mu$, where $\omega_\pm$ is the frequency splitting between the $|0\rangle$ and $|\pm\rangle$ states. The Hamiltonian, in this case, is an XY-interaction between $S = 1$ particles,

$$H_{\text{eff}} = \sum_{i<j} \frac{J_{i,j}}{4}(S_i^+ S_j^- + S_i^- S_j^+) + \sum_{i,m} V_{i,m}[S_i^z - (S_i^z)^2], \tag{6.1}$$

where $S_i^\pm$ are raising and lowering operators and the matrix $V_{i,m}$ is a local field term proportional to the phononic excitations in the ion chain. These local field terms can be eliminated by the addition of two more beat note frequencies at $\omega_- - \mu$ and $\omega_+ + \mu$, which generate a long-range Ising interaction $H = \sum_{i<j} J_{i,j} S_i^x S_j^x$ from a generalization of the Mølmer–Sørensen scheme used for simulating $S = 1/2$ chains [28].

---

[1]These two terms are temporally separated, because additional $\pi/2$ pulses are necessary to rotate the light-shift-generated σ_i^z disorder into the x-direction [21]. The Floquet evolution is equivalent to their simultaneous application, because $[H_2, H_3] = 0$.

12

rsta.royalsocietypublishing.org *Phil. Trans. R. Soc. A* **375**: 20170107

We have observed both coherent quench dynamics between two interacting $S = 1$ ions and adiabatic state preparation in chains of two to four spins by ramping down a global $(S^z)^2$ term [95]. Using our individual addressing laser, we could generate controllable terms of the form $\alpha S_i^z + \beta (S_i^z)^2$ in order to engineer a disordered $S = 1$ chain. This provides a toolbox for $S = 1$ quantum simulations as complete as that for $S = 1/2$, and opens the door to experiments studying localization in integer-spin chains [98,99].

So far, all the experiments described here have been performed on relatively small system sizes of up to 22 spins. Most of the observations can be verified using exact or approximate numerical techniques, including exact diagonalization or the density matrix renormalization group. This has provided an excellent opportunity to demonstrate the capability of trapped ion quantum simulation, while benchmarking their performance on these small systems. However, once the system sizes are increased beyond approximately 30 spins, exact calculations become impossible on highly excited and entangled states like MBL. In this case, larger experiments with well-controlled interactions that scale efficiently with system size are necessary for verifying the numerical calculations and observing new phenomena in large condensed-matter-like systems.

Efforts are underway to dramatically increase the number of ions in a linear crystal and achieve these goals. A current limitation in our experiments is the residual background gas molecules in the vacuum chamber, which can collide with and destroy our long and fragile trapped ion chain. One solution is to engineer a cryogenically pumped ion trap chamber, which promises to have the background pressure and collision rate reduced by orders of magnitude. We have demonstrated that we can trap up to 120 ions in a linear configuration for hours at a time, an important step towards simulating long-range spin models in large systems. By combining this larger system with the techniques for Hamiltonian control developed thus far, we hope to push into the regime of 'quantum supremacy', where our experiments can help understand complex many-body systems in ways inaccessible to current numerical techniques.

References

1. Feynman RP. 1998 *Statistical mechanics: a set of lectures*. Boulder, CO: Westview Press.
2. Cazalilla MA, Rigol M. 2010 Focus on dynamics and thermalization in isolated quantum many-body systems. *New J. Phys.* **12**, 055006. (doi:10.1088/1367-2630/12/5/055006)
3. Polkovnikov A, Sengupta K, Silva A, Vengalattore M. 2011 Colloquium: Nonequilibrium dynamics of closed interacting quantum systems. *Rev. Mod. Phys.* **83**, 863–883. (doi:10.1103/RevModPhys.83.863)
4. D'Alessio L, Kafri Y, Polkovnikov A, Rigol M. 2016 From quantum chaos and eigenstate thermalization to statistical mechanics and thermodynamics. *Adv. Phys.* **65**, 239–362. (doi:10.1080/00018732.2016.1198134)
5. Deutsch JM. 1991 Quantum statistical mechanics in a closed system. *Phys. Rev. A* **43**, 2046–2049. (doi:10.1103/PhysRevA.43.2046)
6. Srednicki M. 1994 Chaos and quantum thermalization. *Phys. Rev. E* **50**, 888–901. (doi:10.1103/PhysRevE.50.888)
7. Rigol M, Dunjko V, Olshanii M. 2008 Thermalization and its mechanism for generic isolated quantum systems. *Nature* **452**, 854–858. (doi:10.1038/nature06838)
8. Basko DM, Aleiner IL, Altshuler BL. 2007 Possible experimental manifestations of the many-body localization. *Phys. Rev. B* **76**, 052203. (doi:10.1103/PhysRevB.76.052203)

9. Oganesyan V, Huse DA. 2007 Localization of interacting fermions at high temperature. *Phys. Rev. B* **75**, 155111. (doi:10.1103/PhysRevB.75.155111)

10. Nandkishore R, Huse DA. 2015 Many-body localization and thermalization in quantum statistical mechanics. *Annu. Rev. Condens. Matter Phys.* **6**, 15–38. (doi:10.1146/annurev-conmatphys-031214-014726)

11. White SR. 1992 Density matrix formulation for quantum renormalization groups. *Phys. Rev. Lett.* **69**, 2863–2866. (doi:10.1103/PhysRevLett.69.2863)

12. Kamenev A, Levchenko A. 2009 Keldysh technique and non-linear σ-model: basic principles and applications. *Adv. Phys.* **58**, 197–319. (doi:10.1080/00018730902850504)

13. Verstraete F, Murg V, Cirac J. 2008 Matrix product states, projected entangled pair states, and variational renormalization group methods for quantum spin systems. *Adv. Phys.* **57**, 143–224. (doi:10.1080/14789940801912366)

14. Kinoshita T, Wenger T, Weiss DS. 2006 A quantum Newton's cradle. *Nature* **440**, 900–903. (doi:10.1038/nature04693)

15. Billy J *et al*. 2008 Direct observation of Anderson localization of matter waves in a controlled disorder. *Nature* **453**, 891–894. (doi:10.1038/nature07000)

16. Gring M *et al*. 2012 Relaxation and prethermalization in an isolated quantum system. *Science* **337**, 1318–1322. (doi:10.1126/science.1224953)

17. Schreiber M, Hodgman SS, Bordia P, Lüschen HP, Fischer MH, Vosk R, Altman E, Schneider U, Bloch I. 2015 Observation of many-body localization of interacting fermions in a quasirandom optical lattice. *Science* **349**, 842–845. (doi:10.1126/science.aaa7432)

18. Kondov SS, McGehee WR, Xu W, DeMarco B. 2015 Disorder-induced localization in a strongly correlated atomic Hubbard gas. *Phys. Rev. Lett.* **114**, 083002. (doi:10.1103/PhysRevLett.114.083002)

19. Kaufman AM, Tai ME, Lukin A, Rispoli M, Schittko R, Preiss PM, Greiner M. 2016 Quantum thermalization through entanglement in an isolated many-body system. *Science* **353**, 794–800. (doi:10.1126/science.aaf6725)

20. Schindler P *et al*. 2013 A quantum information processor with trapped ions. *New J. Phys.* **15**, 123012. (doi:10.1088/1367-2630/15/12/123012)

21. Lee AC, Smith J, Richerme P, Neyenhuis B, Hess PW, Zhang J, Monroe C. 2016 Engineering large Stark shifts for control of individual clock state qubits. *Phys. Rev. A* **94**, 042308. (doi:10.1103/PhysRevA.94.042308)

22. Monz T *et al*. 2011 14-qubit entanglement: creation and coherence. *Phys. Rev. Lett.* **106**, 130506. (doi:10.1103/PhysRevLett.106.130506)

23. Debnath S, Linke NM, Figgatt C, Landsman KA, Wright K, Monroe C. 2016 Demonstration of a small programmable quantum computer with atomic qubits. *Nature* **536**, 63–66. (doi:10.1038/nature18648)

24. Myerson AH *et al*. 2008 High-fidelity readout of trapped-ion qubits. *Phys. Rev. Lett.* **100**, 200502. (doi:10.1103/PhysRevLett.100.200502)

25. Hemmerling B, Gebert F, Wan Y, Schmidt PO. 2012 A novel, robust quantum detection scheme. *New J. Phys.* **14**, 023043. (doi:10.1088/1367-2630/14/2/023043)

26. Monroe C *et al*. 2013 Quantum networks with atoms and photons. *J. Phys. Conf. Ser.* **467**, 012008. (doi:10.1088/1742-6596/467/1/012008)

27. Blatt R, Roos CF. 2012 Quantum simulations with trapped ions. *Nat. Phys.* **8**, 277–284. (doi:10.1038/nphys2252)

28. Mølmer K, Sørensen A. 1999 Multiparticle entanglement of hot trapped ions. *Phys. Rev. Lett.* **82**, 1835–1838. (doi:10.1103/PhysRevLett.82.1835)

29. Porras D, Cirac JI. 2004 Effective quantum spin systems with trapped ions. *Phys. Rev. Lett.* **92**, 207901. (doi:10.1103/PhysRevLett.92.207901)

30. Major F, Gheorghe V, Werth G 2005 *Charged particle traps: physics and techniques of charged particle field confinement*. Springer Series on Atomic, Optical, and Plasma Physics, vol. 37. Berlin, Germany: Springer.

31. Olmschenk S, Younge KC, Moehring DL, Matsukevich DN, Maunz P, Monroe C. 2007 Manipulation and detection of a trapped Yb^+ hyperfine qubit. *Phys. Rev. A* **76**, 052314. (doi:10.1103/PhysRevA.76.052314)

32. Noek R, Vrijsen G, Gaultney D, Mount E, Kim T, Maunz P, Kim J. 2013 High speed, high fidelity detection of an atomic hyperfine qubit. *Opt. Lett.* **38**, 4735. (doi:10.1364/OL.38.004735)

33. Zhu S-L, Monroe C, Duan L-M. 2006 Trapped ion quantum computation with transverse phonon modes. *Phys. Rev. Lett.* **97**, 050505. (doi:10.1103/PhysRevLett.97.050505)
34. Kim K, Chang M-S, Islam R, Korenblit S, Duan L-M, Monroe C. 2009 Entanglement and tunable spin–spin couplings between trapped ions using multiple transverse modes. *Phys. Rev. Lett.* **103**, 120502. (doi:10.1103/PhysRevLett.103.120502)
35. Hayes D *et al.* 2010 Entanglement of atomic qubits using an optical frequency comb. *Phys. Rev. Lett.* **104**, 140501. (doi:10.1103/PhysRevLett.104.140501)
36. Islam R *et al.* 2014 Beat note stabilization of mode-locked lasers for quantum information processing. *Opt. Lett.* **39**, 3238. (doi:10.1364/OL.39.003238)
37. Lee A. 2016 Engineering a quantum many-body hamiltonian with trapped ions. PhD thesis, University of Maryland.
38. Senko C, Smith J, Richerme P, Lee A, Campbell WC, Monroe C. 2014 Coherent imaging spectroscopy of a quantum many-body spin system. *Science* **345**, 430–433. (doi:10.1126/science.1251422)
39. Smith J, Lee A, Richerme P, Neyenhuis B, Hess PW, Hauke P, Heyl M, Huse DA, Monroe C. 2016 Many-body localization in a quantum simulator with programmable random disorder. *Nat. Phys.* **12**, 907–911. (doi:10.1038/nphys3783)
40. Jurcevic P, Lanyon BP, Hauke P, Hempel C, Zoller P, Blatt R, Roos CF. 2014 Quasiparticle engineering and entanglement propagation in a quantum many-body system. *Nature* **511**, 202–205. (doi:10.1038/nature13461)
41. Korenblit S *et al.* 2012 Quantum simulation of spin models on an arbitrary lattice with trapped ions. *New J. Phys.* **14**, 095024. (doi:10.1088/1367-2630/14/9/095024)
42. Campbell WC, Mizrahi J, Quraishi Q, Senko C, Hayes D, Hucul D, Matsukevich DN, Maunz P, Monroe C. 2010 Ultrafast gates for single atomic qubits. *Phys. Rev. Lett.* **105**, 090502. (doi:10.1103/PhysRevLett.105.090502)
43. Staanum P, Drewsen M. 2002 Trapped-ion quantum logic utilizing position-dependent ac Stark shifts. *Phys. Rev. A* **66**, 040302. (doi:10.1103/PhysRevA.66.040302)
44. Mizrahi J, Senko C, Neyenhuis B, Johnson KG, Campbell WC, Conover CWS, Monroe C. 2013 Ultrafast spin–motion entanglement and interferometry with a single atom. *Phys. Rev. Lett.* **110**, 203001. (doi:10.1103/PhysRevLett.110.203001)
45. Neyenhuis B, Zhang J, Hess P, Smith J, Lee A, Richerme P, Gong Z-X, Gorshkov A, Monroe C. 2017 Observation of prethermalization in long-range interacting spin chains. *Sci. Adv.* **3**, e1700672. (doi:10.1126/sciadv.1700672)
46. Jurcevic P, Hauke P, Maier C, Hempel C, Lanyon BP, Blatt R, Roos CF. 2015 Spectroscopy of interacting quasiparticles in trapped ions. *Phys. Rev. Lett.* **115**, 100501. (doi:10.1103/PhysRevLett.115.100501)
47. Basko D, Aleiner I, Altshuler B. 2006 Metal–insulator transition in a weakly interacting many-electron system with localized single-particle states. *Ann. Phys.* **321**, 1126–1205. (doi:10.1016/j.aop.2005.11.014)
48. Anderson PW. 1958 Absence of diffusion in certain random lattices. *Phys. Rev.* **109**, 1492–1505. (doi:10.1103/PhysRev.109.1492)
49. Wiersma DS, Bartolini P, Lagendijk A, Righini R. 1997 Localization of light in a disordered medium. *Nature* **390**, 671–673. (doi:10.1038/37757)
50. Roati G, D'Errico C, Fallani L, Fattori M, Fort C, Zaccanti M, Modugno G, Modugno M, Inguscio M. 2008 Anderson localization of a non-interacting Bose–Einstein condensate. *Nature* **453**, 895–898. (doi:10.1038/nature07071)
51. Kondov SS, McGehee WR, Zirbel JJ, DeMarco B. 2011 Three-dimensional Anderson localization of ultracold matter. *Science* **334**, 66–68. (doi:10.1126/science.1209019)
52. Schwartz T, Bartal G, Fishman S, Segev M. 2007 Transport and Anderson localization in disordered two-dimensional photonic lattices. *Nature* **446**, 52–55. (doi:10.1038/nature05623)
53. Dalichaouch R, Armstrong JP, Schultz S, Platzman PM, McCall SL. 1991 Microwave localization by two-dimensional random scattering. *Nature* **354**, 53–55. (doi:10.1038/354053a0)
54. Hu H, Strybulevych A, Page JH, Skipetrov SE, van Tiggelen BA. 2008 Localization of ultrasound in a three-dimensional elastic network. *Nat. Phys.* **4**, 945–948. (doi:10.1038/nphys1101)
55. Luitz DJ, Laflorencie N, Alet F. 2015 Many-body localization edge in the random-field Heisenberg chain. *Phys. Rev. B* **91**, 081103. (doi:10.1103/PhysRevB.91.081103)

15

rsta.royalsocietypublishing.org Phil. Trans. R. Soc. A 375: 20170107

56. Hauke P, Heyl M. 2015 Many-body localization and quantum ergodicity in disordered long-range Ising models. *Phys. Rev. B* **92**, 134204. (doi:10.1103/PhysRevB.92.134204)

57. Iyer S, Oganesyan V, Refael G, Huse DA. 2013 Many-body localization in a quasiperiodic system. *Phys. Rev. B* **87**, 134202. (doi:10.1103/PhysRevB.87.134202)

58. Wu Y-L, Das Sarma S. 2016 Understanding analog quantum simulation dynamics in coupled ion-trap qubits. *Phys. Rev. A* **93**, 022332. (doi:10.1103/PhysRevA.93.022332)

59. Burin AL. 2015 Localization in a random *XY* model with long-range interactions: intermediate case between single-particle and many-body problems. *Phys. Rev. B* **92**, 104428. (doi:10.1103/PhysRevB.92.104428)

60. Bordia P, Lüschen HP, Hodgman SS, Schreiber M, Bloch I, Schneider U. 2016 Coupling identical one-dimensional many-body localized systems. *Phys. Rev. Lett.* **116**, 140401. (doi:10.1103/PhysRevLett.116.140401)

61. Lüschen HP, Bordia P, Hodgman SS, Schreiber M, Sarkar S, Daley AJ, Fischer MH, Altman E, Bloch I. 2017 Signatures of many-body localization in a controlled open quantum system. *Phys. Rev. X* **7**, 011034. (doi:10.1103/PhysRevX.7.011034)

62. Reimann P. 2008 Foundation of statistical mechanics under experimentally realistic conditions. *Phys. Rev. Lett.* **101**, 190403. (doi:10.1103/PhysRevLett.101.190403)

63. Larson J. 2013 Integrability versus quantum thermalization. *J. Phys. B., At. Mol. Opt. Phys.* **46**, 224016. (doi:10.1088/0953-4075/46/22/224016)

64. Manmana SR, Wessel S, Noack RM, Muramatsu A. 2007 Strongly correlated fermions after a quantum quench. *Phys. Rev. Lett.* **98**, 210405. (doi:10.1103/PhysRevLett.98.210405)

65. Kiendl T, Marquardt F. 2017 Many-particle dephasing after a quench. *Phys. Rev. Lett.* **118**, 130601. (doi:10.1103/PhysRevLett.118.130601)

66. Berges J, Borsányi S, Wetterich C. 2004 Prethermalization. *Phys. Rev. Lett.* **93**, 142002. (doi:10.1103/PhysRevLett.93.142002)

67. Langen T *et al.* 2015 Experimental observation of a generalized Gibbs ensemble. *Science* **348**, 207–211. (doi:10.1126/science.1257026)

68. Rigol M, Dunjko V, Yurovsky V, Olshanii M. 2007 Relaxation in a completely integrable many-body quantum system: an *ab initio* study of the dynamics of the highly excited states of 1D lattice hard-core bosons. *Phys. Rev. Lett.* **98**, 050405. (doi:10.1103/PhysRevLett.98.050405)

69. Gong Z-X, Duan L-M. 2013 Prethermalization and dynamic phase transition in an isolated trapped ion spin chain. *New J. Phys.* **15**, 113051. (doi:10.1088/1367-2630/15/11/113051)

70. Marcuzzi M, Marino J, Gambassi A, Silva A. 2013 Prethermalization in a nonintegrable quantum spin chain after a quench. *Phys. Rev. Lett.* **111**, 197203. (doi:10.1103/PhysRevLett.111.197203)

71. Richerme P, Gong Z-X, Lee A, Senko C, Smith J, Foss-Feig M, Michalakis S, Gorshkov AV, Monroe C. 2014 Non-local propagation of correlations in quantum systems with long-range interactions. *Nature* **511**, 198–201. (doi:10.1038/nature13450)

72. Ponte P, Chandran A, Papić Z, Abanin DA. 2015 Periodically driven ergodic and many-body localized quantum systems. *Ann. Phys.* **353**, 196–204. (doi:10.1016/j.aop.2014.11.008)

73. D'Alessio L, Rigol M. 2014 Long-time behavior of isolated periodically driven interacting lattice systems. *Phys. Rev. X* **4**, 041048. (doi:10.1103/PhysRevX.4.041048)

74. Chirikov B, Izrailev F, Shepelyansky D. 1981 Dynamical stochasticity in classical and quantum mechanics. *Sov. Sci. Rev. Sect. C* **2**, 209.

75. Fishman S, Grempel DR, Prange RE. 1982 Chaos, quantum recurrences, and Anderson localization. *Phys. Rev. Lett.* **49**, 509–512. (doi:10.1103/PhysRevLett.49.509)

76. Khemani V, Lazarides A, Moessner R, Sondhi SL. 2016 Phase structure of driven quantum systems. *Phys. Rev. Lett.* **116**, 250401. (doi:10.1103/PhysRevLett.116.250401)

77. Potter AC, Morimoto T, Vishwanath A. 2016 Classification of interacting topological Floquet phases in one dimension. *Phys. Rev. X* **6**, 041001. (doi:10.1103/PhysRevX.6.041001)

78. Sacha K. 2015 Modeling spontaneous breaking of time-translation symmetry. *Phys. Rev. A* **91**, 033617. (doi:10.1103/PhysRevA.91.033617)

79. Else DV, Bauer B, Nayak C. 2016 Floquet time crystals. *Phys. Rev. Lett.* **117**, 090402. (doi:10.1103/PhysRevLett.117.090402)

80. Yao NY, Potter AC, Potirniche I-D, Vishwanath A. 2017 Discrete time crystals: rigidity, criticality, and realizations. *Phys. Rev. Lett.* **118**, 030401. (doi:10.1103/PhysRevLett.118.030401)

16

rsta.royalsocietypublishing.org *Phil. Trans. R. Soc. A* **375**: 20170107

81. Lazarides A, Das A, Moessner R. 2014 Equilibrium states of generic quantum systems subject to periodic driving. *Phys. Rev. E* **90**, 012110. (doi:10.1103/PhysRevE.90.012110)

82. Wilczek F. 2013 Superfluidity and space-time translation symmetry breaking. *Phys. Rev. Lett.* **111**, 250402. (doi:10.1103/PhysRevLett.111.250402)

83. Bruno P. 2013 Impossibility of spontaneously rotating time crystals: a no-go theorem. *Phys. Rev. Lett.* **111**, 070402. (doi:10.1103/PhysRevLett.111.070402)

84. Nozières P. 2013 Time crystals: can diamagnetic currents drive a charge density wave into rotation? *Europhys. Lett.* **103**, 57008. (doi:10.1209/0295-5075/103/57008)

85. Watanabe H, Oshikawa M. 2015 Absence of quantum time crystals. *Phys. Rev. Lett.* **114**, 251603. (doi:10.1103/PhysRevLett.114.251603)

86. Zhang J *et al.* 2017 Observation of a discrete time crystal. *Nature* **543**, 217–220. (doi:10.1038/nature21413)

87. Choi S *et al.* 2017 Observation of discrete time-crystalline order in a disordered dipolar many-body system. *Nature* **543**, 221–225. (doi:10.1038/nature21426)

88. De Roeck W, Huveneers F. 2017 Stability and instability towards delocalization in many-body localization systems. *Phys. Rev. B* **85**, 155129. (doi:10.1103/PhysRevB.95.155129)

89. Britton JW, Sawyer BC, Keith AC, Wang C-CJ, Freericks JK, Uys H, Biercuk MJ, Bollinger JJ. 2012 Engineered two-dimensional Ising interactions in a trapped-ion quantum simulator with hundreds of spins. *Nature* **484**, 489–492. (doi:10.1038/nature10981)

90. Bohnet JG, Sawyer BC, Britton JW, Wall ML, Rey AM, Foss-Feig M, Bollinger JJ. 2016 Quantum spin dynamics and entanglement generation with hundreds of trapped ions. *Science* **352**, 1297–1301. (doi:10.1126/science.aad9958)

91. Yoshimura B, Stork M, Dadic D, Campbell WC, Freericks JK. 2015 Creation of two-dimensional Coulomb crystals of ions in oblate Paul traps for quantum simulations. *EPJ Quantum Technol.* **2**, 2. (doi:10.1140/epjqt14)

92. Richerme P. 2016 Two-dimensional ion crystals in radio-frequency traps for quantum simulation. *Phys. Rev. A* **94**, 032320. (doi:10.1103/PhysRevA.94.032320)

93. Haldane FDM. 1983 Nonlinear field theory of large-spin Heisenberg antiferromagnets: semiclassically quantized solitons of the one-dimensional easy-axis Néel state. *Phys. Rev. Lett.* **50**, 1153–1156. (doi:10.1103/PhysRevLett.50.1153)

94. Affleck I, Kennedy T, Lieb EH, Tasaki H. 1988 Valence bond ground states in isotropic quantum antiferromagnets. *Commun. Math. Phys.* **115**, 477–528. (doi:10.1007/BF01218021)

95. Senko C, Richerme P, Smith J, Lee A, Cohen I, Retzker A, Monroe C. 2015 Realization of a quantum integer-spin chain with controllable interactions. *Phys. Rev. X* **5**, 021026. (doi:10.1103/PhysRevX.5.021026)

96. Cohen I, Retzker A. 2014 Proposal for verification of the Haldane phase using trapped ions. *Phys. Rev. Lett.* **112**, 040503. (doi:10.1103/PhysRevLett.112.040503)

97. Cohen I, Richerme P, Gong Z-X, Monroe C, Retzker A. 2015 Simulating the Haldane phase in trapped-ion spins using optical fields. *Phys. Rev. A* **92**, 012334. (doi:10.1103/PhysRevA.92.012334)

98. Graß T, Juliá-Díaz B, Kuś M, Lewenstein M. 2013 Quantum chaos in SU(3) models with trapped ions. *Phys. Rev. Lett.* **111**, 090404. (doi:10.1103/PhysRevLett.111.090404)

99. Calvanese Strinati M, Mazza L, Endres M, Rossini D, Fazio R. 2016 Destruction of string order after a quantum quench. *Phys. Rev. B* **94**, 024302. (doi:10.1103/PhysRevB.94.024302)